

Thermal Convection in a Central Force Field Mediated by Sound

John P. Koulakis¹,* Yotam Ofek, Seth Pree¹,† and Seth Putterman

Department of Physics and Astronomy, University of California Los Angeles, Los Angeles, California 90095, USA

 (Received 9 July 2022; revised 22 October 2022; accepted 22 November 2022; published 20 January 2023)

Convection in radial force fields is a fundamental process behind weather on Earth and the Sun, as well as magnetic dynamo action in both. Until now, benchtop experiments have been unable to study convection in radial force fields due to the inability to generate radial forces of sufficient strength. Recently, it has been appreciated that sound, when averaged over many cycles, exerts a force on density gradients in the gas it travels through. The acoustic radiation pressure on thermal gradients draws cooler gas to regions with large time-averaged acoustic velocity and can be modeled as an effective acoustic gravity. We have constructed a system which generates a high amplitude, spherically symmetric acoustic wave in a rotating spherical bulb containing weakly ionized sulfur gas. Without sound, the gas stratifies itself into an initial state with the warmest gas near the center of the bulb, and the coolest gas near the bulb surface. When the sound is initiated, the acoustic radiation pressure is not balanced and a convective instability is triggered. With high speed videography, we observe the initial shape and growth rate of the most unstable mode at various acoustic amplitudes. Acoustic and rotational forces both contribute to the detailed mode shape, which changes qualitatively at low amplitudes where acoustic forces no longer surpass rotational ones everywhere in the bulb.

DOI: 10.1103/PhysRevLett.130.034002

Introduction.—Convection in spherical, rotating, systems is fundamental to processes in stars and planets and is ubiquitous throughout our universe. It partially determines, for example, solar flares and space weather [1], granulation on the Sun's surface [2], weather on Earth, and magnetic dynamo action in both [3,4]. Convection experiments in spherical systems with a radial force are difficult to realize due to the challenges of arranging for a radial force that overwhelms buoyancy (gravity) at Earth's surface. To date, the only viable option has been the dielectrophoretic force, which relies on strong alternating electric fields and variations in a fluid's dielectric constant with temperature [5–8]. However, because of its inherent weakness, experiments were forced into a microgravity environment, with all associated challenges and expenses [9–13].

Recent advances in generalizing acoustic radiation pressure theory to encompass inhomogeneous fluids [14,15] have found that sound exerts a nonzero, time-averaged force on density *gradients*. In the simplest case of an ideal gas, the leading order slow dynamics are described by [14,16]

$$\frac{\partial}{\partial t}(\bar{\rho}\bar{\mathbf{v}}) + \nabla(\bar{\rho}\bar{\mathbf{v}}\bar{\mathbf{v}}) = -\nabla\bar{P}^{\text{eff}} - \frac{\langle v_1^2 \rangle}{2}\nabla\bar{\rho} + \bar{\rho}\mathbf{g} + \eta\nabla^2\bar{\mathbf{v}} \quad (1)$$

where $\bar{\rho}$, \bar{P}^{eff} , $\bar{\mathbf{v}}$ are the time-averaged density, effective pressure, and velocity, respectively; \mathbf{g} is a gravitational field, $\langle v_1^2 \rangle$ is the time-averaged square of the acoustic velocity, and η is the viscosity. Aside from a modification of

the pressure, the sound field, at second order, leads to a pycnoclinic acoustic radiation force given by $-\langle v_1^2 \rangle \nabla\bar{\rho}/2$. That this term leads to an acoustic gravity $\mathbf{g}_{\text{ac}} = \nabla\langle v_1^2 \rangle/2$ can be motivated by taking the curl of Eq. (1) neglecting viscosity and convection to obtain

$$\frac{\partial}{\partial t}\nabla \times (\bar{\rho}\bar{\mathbf{v}}) = [\mathbf{g} + \nabla\langle v_1^2 \rangle/2] \times \nabla\bar{\rho}, \quad (2)$$

and noting that $\nabla\langle v_1^2 \rangle/2$ generates vorticity in the same manner as \mathbf{g} . This argument is equivalent to that made for thermovibrational [17] and dielectrophoretic [8–10] forces, where, in particular, the force on dielectric gradients $-E^2\nabla\epsilon/2$ for permittivity ϵ and electric field E forms the basis of the “electrostatic gravity” $\epsilon\nabla E^2/2$ in the microgravity experiments. In the case of acoustic gravity, dense gas falls towards regions of high acoustic velocity, and with a spherical standing wave, one can arrange for an acoustic gravity that points radially.

Herein we describe experiments on convective instability triggered by the turn-on of a radial acoustic gravity field. Figure 1(a) is one frame of a high speed video capturing the flow of hot sulfur gas immediately after a spherical acoustic wave is excited in a 3 cm diameter bulb that simultaneously rotates. The overlaid convection cells are axisymmetric and determined by studying videos available in the Supplemental Material [18].

The sulfur gas is heated volumetrically by microwaves. Sound is excited by amplitude modulating the microwave, and can briefly reach amplitudes that imply an acoustic

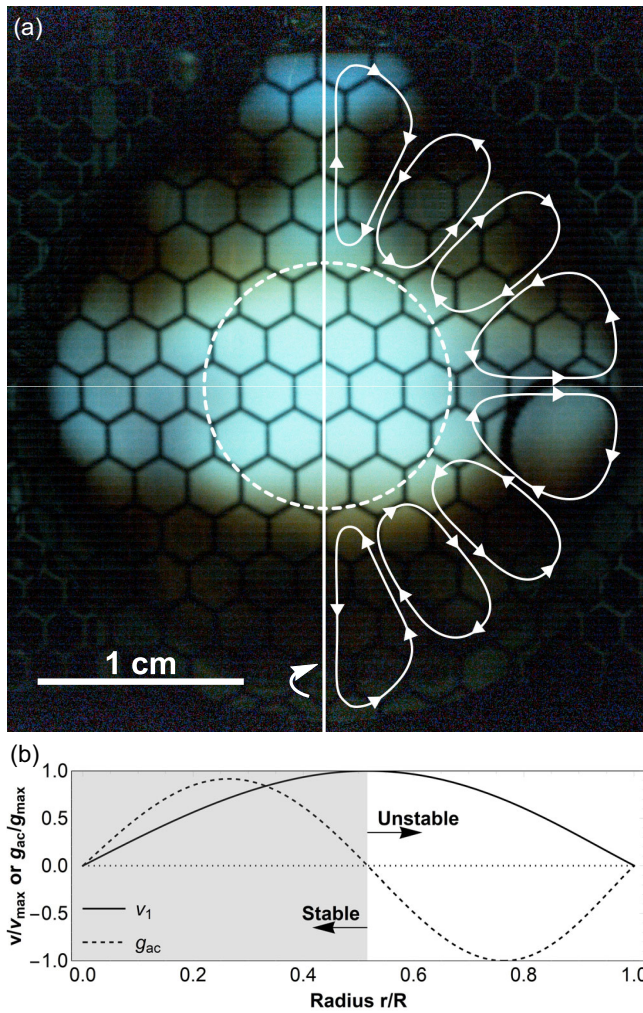


FIG. 1. (a) Convection cells driven by the radial “acoustic gravity” of a spherical standing sound wave in a rotating sulfur plasma bulb. Direction of flow indicated by the streamlines has been extracted from high speed video available in the Supplemental Material. Cells are axisymmetric about the rotation axis (vertical line centered in figure). The hexagonal pattern visible in the image is the shadow of the metal mesh which forms the microwave cavity. (b) The acoustic velocity and effective gravity as a function of radius. Note that the acoustic gravity changes sign at the velocity antinode, which occurs at nearly half the bulb radius (dashed white circle). Since the plasma is volumetrically heated internally and is hottest at the center, the region inside of the antinode is stable, while the region outside of the velocity antinode is unstable. Convection in the outer zone is similar to Rayleigh-Bénard convection in a time-varying, spherical, acoustic gravity field.

gravity field that is $\sim 1000\times$ stronger than Earth’s gravity [19]. As shown in Fig. 1(b), the lowest order spherically symmetric acoustic mode has a velocity profile similar to a half-sine wave with maximum (antinode) at about half the bulb radius [20]. This means the acoustic gravity of that mode has a profile similar to a full sine wave, changing sign at the antinode. From the antinode inwards (the inner zone),

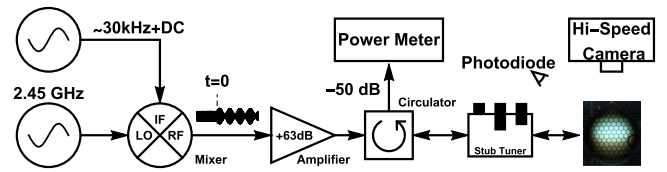


FIG. 2. Block diagram of microwave system which heats the sulfur and generates sound. Amplitude modulation of the microwave power generates sound waves inside the bulb. The acoustic gravity of the standing sound wave destabilizes the stratification of the quiescent bulb and the growth of the most unstable mode is captured on high-speed video as a function of microwave modulation depth.

the gas is stably stratified with the hottest gas at the center. Conversely, the region from the antinode outwards (the outer zone) is characterized by instability [19] best described as Rayleigh-Bénard convection in a time-varying acoustic gravity field, but with an internal source of heat and lacking one boundary [21,22]. Convection in the outer zone dramatically increases thermal transport to the glass, resulting in a frequency shift of the resonant mode [23], and measurably hotter glass temperature [19].

This Letter focuses on the initial motion of the fluid immediately after exciting the sound wave to better understand the most unstable, fastest growing convective mode. We have observed the instability at various acoustic amplitudes at fixed rotation rate, and have identified a transition in the modal structure at low amplitudes. We interpret the transition in terms of a balance of acoustic and rotational forces at the equator.

Experiment.—A block diagram of the experimental system is shown in Fig. 2. It has been described extensively in various forms elsewhere [19,24–26] and here we describe aspects specific to this Letter. The plasma bulb sits inside a cylindrical microwave cavity made of hexagonal metal mesh which simultaneously confines the microwave and allows visualization of the convection. Initially, the sulfur plasma is heated by an unmodulated 2.45 GHz microwave signal amplified up to 2 kW by a solid state linear amplifier (Empower 2180) to a final molecular density of $\sim 2 \times 10^{19} \text{ cm}^{-3}$ and $\sim 10^{-5}$ ionization fraction [27,28]. Impedance matching is achieved with a three-stub tuner. Once quiescent conditions are reached, the acoustic resonance frequency of the bulb’s lowest order spherically symmetric mode (near 30 kHz) is determined by imposing a small $\sim 2\%$ modulation depth and sweeping the modulation frequency until the plasma is observed to flicker [20]. The spherical symmetry of the acoustic mode has been confirmed with direct observation [19] and matching of the ultrasonic resonance spectrum with theory [20]. The amplitude modulation is switched off and the plasma is allowed to return to the quiescent state. While off, the modulation frequency is set to match the resonance and the modulation depth is increased to 40%–100%. A high

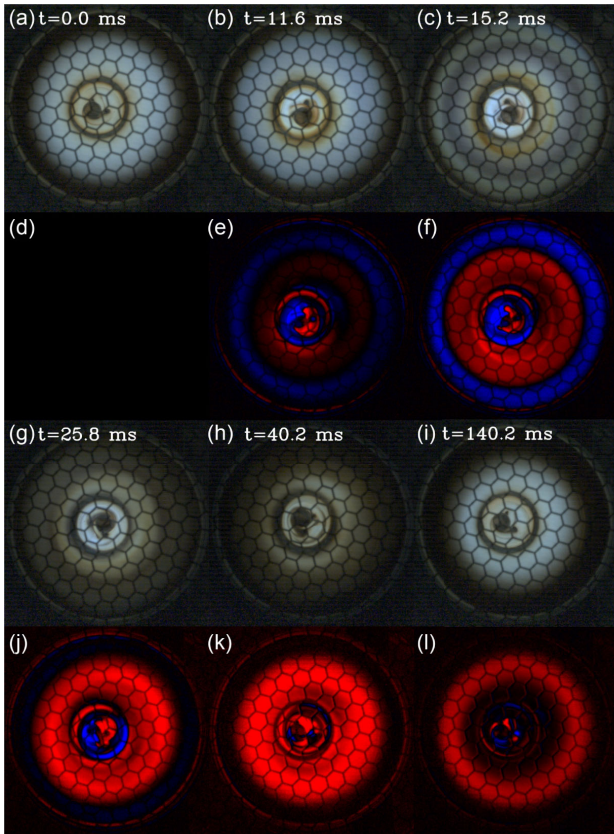


FIG. 3. Top view of instability evolution indicates the instability is axially symmetric. The feature visible at the center of the bulb in every frame is a pontil mark on the bulb from glass-blowing. Panels (a)–(c) and (g)–(i) are frames of high speed video while panels (d)–(f) and (j)–(l) are false color images of the difference in brightness from panel a. Red (blue) coloring indicates the pixel value is lower (higher) than it was in panel (a).

speed video camera (Vision Research Phantom v2640) operating at 5000 frames per second begins recording, and the instability is triggered by reactivating the modulation. The growth of the most unstable mode is captured for various acoustic amplitudes at a fixed bulb rotation rate of 17 Hz. Rotation of the bulb is essential for achieving steady-state, quiescent conditions; without it the plasma is chaotic, violently flickers, and is prone to sudden extinction [29].

Results and discussion.—Figures 3 and 4 show high speed video frames from two distinct but analogous events viewed from the top (along the rotation axis) and side, respectively. The first and third rows of each figure show the frames in actual color while the second and fourth rows are false color images of the difference in pixel brightness from the first frame. Panel (a) in both figures shows the plasma in the quiescent state before the acoustic gravity is initiated. From the top view (Fig. 3) the flow is seen to be axially symmetric about the rotation axis. In panel Fig. 3(b) the luminous radius of the plasma has moved out leaving dimmer pixels near the center. A clear, dim ring encircling

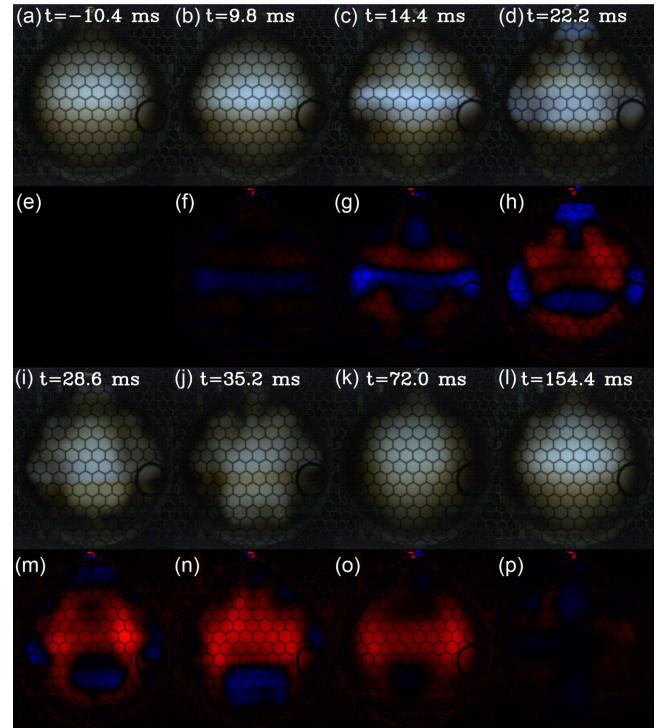


FIG. 4. Side view of instability evolution. Panels (a)–(d) and (i)–(l) are frames of high speed video while panels (e)–(h) and (m)–(p) are false color images of the difference in brightness from panel (a). Red (blue) coloring indicates the pixel value is lower (higher) than it was in panel (a).

the inner zone in Fig. 3(c) indicates the outer zone has inverted bringing the hot gas towards the glass and the cooler gas towards the velocity antinode. Heat flows into the glass leaving dimmer plasma in the outer zone [Figs. 3(g) and 3(h)], shifting the resonant frequency of the bulb, and detuning it from the drive. By panel Fig. 3(i), the acoustic amplitude and acoustic gravity have decayed sufficiently to allow the gas to heat back up to the quiescent state. Viewing the event from the side, Fig. 4, elucidates the polar angular structure of the flow. The outward motion visible in Figs. 3(b) and 3(c) is outward flow at the equator. Also, there is outward flow at the poles and midlatitudes (at about 45°) with the return flow between. The outward plumes form an eight-pointed star seen in panel Fig. 4(c), some of which evolve into mushroom shaped features after interacting with the glass in panel Fig. 4(d). Panels Figs. 4(i)–4(l) show the cooling and recovery. The inner zone is distinctly visible as a bright, unmoving ball once the outer zone cools, as in Figs. 3(h) and 4(d).

The axisymmetric convection cells we observe are similar in character to those predicted for thermal convection in spherical shells with normal gravity [30], and in planar systems with acoustic gravity [16]. The linear theory for the modes with spherical acoustic gravity has not been developed. Consistent formation of outward plumes at the poles and equator implies spherical symmetry has been

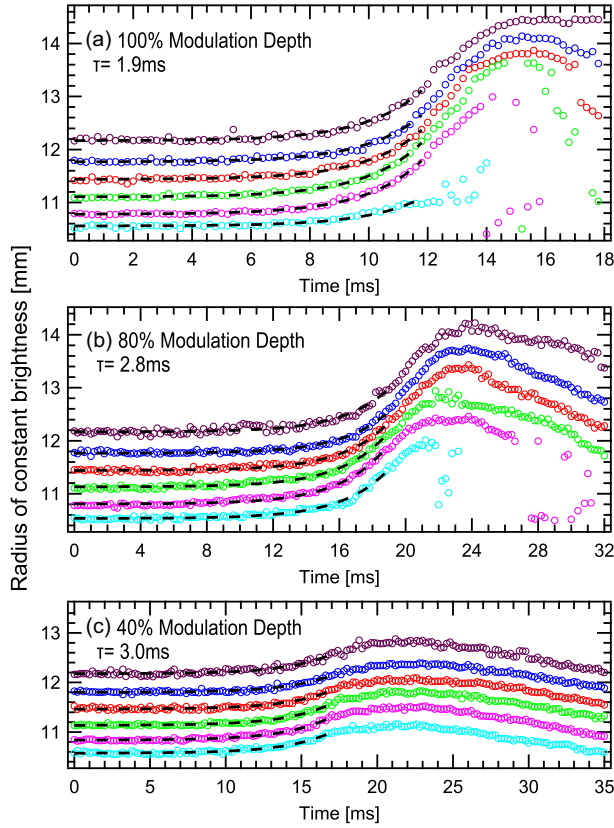


FIG. 5. Timescales of convection onset are extracted from the top view high frame rate videos by finding the radius of circles where the brightness drops below a threshold value over time and fitting exponentials (dashed black curves). Each color is a different threshold, with inner contours corresponding to higher thresholds (brighter pixels). The growth time constant of the instability at 100% (a), 80% (b), and 40% (c) modulation depth is 1.9 ms, 2.8 ms, and 3.0 ms respectively.

sufficiently broken to pin the orientation of the mode. Rotation of the bulb can give a preferred direction, as can asymmetry in the quiescent state due to Earth’s gravity, asphericity of the bulb itself, wobble of the rotation axis, or small amplitudes of other acoustic modes.

Extraction of the mode’s growth time is facilitated by the symmetry of the flow when viewed from the top. An algorithm processes the videos by finding the brightness of pixels as a function of the distance from the plasma center, which is a monotonically decreasing curve at early times. It then finds the radius at which the plasma brightness drops below a set threshold. Plotting these radii over time for various thresholds or, equivalently, the initial position, gives the curves in Fig. 5. Since the growth time of a convection mode does not vary in space, each curve must have the same time constant. To ensure this, a least squares fit is done simultaneously to all curves, forcing their time constants to be equal. The resulting fits are the dashed black curves overlaid on the data. The growth time constants are 1.9 ms, 2.8 ms, and 3.0 ms for 100%, 80%, and 40% modulation depth, respectively.

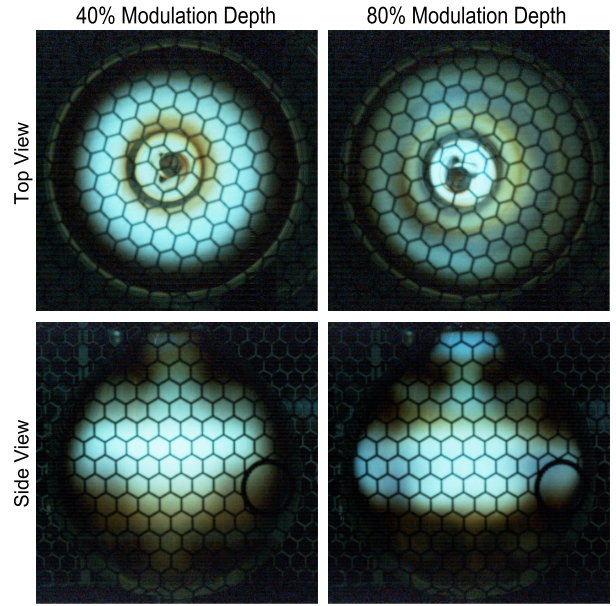


FIG. 6. Although the growth times of the convective modes at 40% and 80% modulation depth are similar, their shape is qualitatively different. This difference is due to a change in the balance of rotational and acoustic forces.

Acoustic gravity and the convective growth rate (inverse time constant) are expected to scale with the square of the acoustic amplitude, or square of the modulation depth [16]. The ratio of the time constants of the 80% and 100% modulation depth runs, $1.9 \text{ ms}/2.8 \text{ ms} \approx 0.68$, is within 7% of the predicted scaling $0.8^2 = 0.64$. This scaling does not hold between 40% and 80%, which have very similar growth times. A qualitative change is observed in the shape of the mode when the modulation depth is increased from 40% to 80% as shown in Fig. 6. At 80% modulation depth, the polar, equatorial, and midlatitude plumes are all clearly visible. But at 40% modulation depth, only the polar plume is distinct. Figure 5(c) shows that although there is some outward motion at the equator, the extent of the motion is greatly reduced compared to that shown in Fig. 5(b) for 80% modulation depth.

This evidence suggests that we are observing a crossover in convection regimes where different forces are dominant. At 80% and 100% modulation depth, acoustic gravity overwhelms rotational forces and the shape of the mode is mainly determined by the spherical force field. At 40% modulation depth, the acoustic gravity is weak enough that centripetal forces at the equator surpass acoustic ones and suppress the equatorial plume.

Conclusion.—The relevance of our experiment to planetary or stellar convection is determined by the dimensionless fluid parameters of our system. Equation (1) may be nondimensionalized according to $\mathbf{r} = R\mathbf{r}^*$, $\mathbf{v} = (\chi/R)\mathbf{v}^*$, $\bar{\rho} = \rho_w\bar{\rho}^*$, $\tau = (R^2/\chi)\tau^*$, and $\langle v_1^2 \rangle = v_{\text{rms}}^2 v_1^{2*}(r^*)$ where R is the bulb radius, χ is the thermal diffusivity, ρ_w is the

density at the glass, v_{rms} is the root-mean-squared acoustic velocity, and the starred parameters are dimensionless. We have replaced the thermal scale here with a density scale which is more natural for our system. The resulting nondimensional parameters are the Prandtl number $\text{Pr} = \eta/(\rho_w \chi) \simeq 0.15$, gravitational Rayleigh number $\text{Ra}_g = gR^3 \rho_w / (\eta \chi) \simeq 5600$, and acoustic Rayleigh number $\text{Ra}_{\text{ac}} = v_{\text{rms}}^2 R^2 \rho_w / (2\eta \chi) \simeq 3 \times 10^6$. Centripetal forces compared to Earth's gravity are parametrized by the Froude number $\text{Fr} = \Omega^2 R / g \simeq 17$ or the acoustic Froude number $\text{Fr}_{\text{ac}} = 2\Omega^2 R^2 / v_{\text{rms}}^2 \simeq 0.026$, where Ω is the rotation rate. The strength of the Coriolis force is parametrized by the Ekman number $\text{Ek} = \eta / (2\rho_w \Omega R^2) \simeq 6 \times 10^{-4}$. These were evaluated with $R = 15$ mm, $\Omega = 2\pi \times 17$ Hz, $v_{\text{rms}}^2 \simeq (20 \text{ m s}^{-1})^2 / 2$, $\eta / \rho_w \simeq 3 \times 10^{-5} \text{ m}^2 \text{ s}^{-1}$, $\chi \simeq 2 \times 10^{-4} \text{ m}^2 \text{ s}^{-1}$ estimated from data in [19,20]. Our peak acoustic Rayleigh number is greater than what is reported for GeoFlow [9,31]. Although these values can be simulated [32], there is a route to upscaling this phenomenon. The plasma is excited via its absorption of the externally applied microwave field. Under the right conditions, the phase of the oscillating absorption coefficient provides a source of gain which will spontaneously amplify and sustain the sound field in the presence of convection [33].

This experiment captures some notoriously difficult aspects of convection. Namely, it is a benchtop system capable of driving thermal convection in a spherical force that overpowers Earth's gravity. The system rotates and is internally heated. It has a factor ~ 2 change in density between the inner and outer limits of the unstable region, going far beyond the Boussinesq approximation into the compressible regime [34]. The effective gravity of the acoustic mode changes sign at about half of the bulb radius and divides the bulb into stable and unstable regions. Further, the plumes in the outer zone transport angular momentum and likely result in some amount of differential rotation. Although this experiment does not exhibit relevant magnetic fields, these features are thought to play a key role in the solar tachocline and the Sun's magnetic cycle. Finally, we note that on the long timescale, the processes discussed here lead to a noisy "steady state" which is representative of conditions that accompany blackout in communication with reentry and hypersonic vehicles [24].

We acknowledge valuable discussions with Nicholas Featherstone and Jonathan Aurnou. This research was initiated with funding from the Defense Advanced Research Projects Agency (DARPA D19AP00015). S. Putterman, J. Koulakis and Y. Ofek are supported in part by the AFOSR (FA9550-21-1-0295). The views, opinions, and/or findings expressed are those of the authors and should not be interpreted as representing the official views or policies of the Department of Defense or the U.S. Government.

*koulakis@physics.ucla.edu

†Present address: Applied Physics and Materials Science, California Institute of Technology, Pasadena, California 91125, USA.

- [1] D. J. Galloway, Y. Uchida, and N. O. Weiss, Generation of coronal currents by the solar convection zone, *Pub. Astron. Soc. Aust.* **18**, 329 (2001).
- [2] N. A. Featherstone and B. W. Hindman, The emergence of solar supergranulation as a natural consequence of rotationally constrained interior convection, *Astrophys. J. Lett.* **830**, L15 (2016).
- [3] P. Olson, Experimental dynamos and the dynamics of planetary cores, *Annu. Rev. Earth Planet Sci.* **41**, 153 (2013).
- [4] S. M. Tobias, The solar dynamo, *Phil. Trans. R. Soc. A* **360**, 2741 (2002).
- [5] L. D. Landau and E. M. Lifshitz, *Electrodynamics of Continuous Media*, 2nd ed. (Butterworth-Heinemann, Burlington, MA, USA, 1984), pp. 59–64.
- [6] B. Chandra and D. E. Smylie, A laboratory model of thermal convection under a central force field, *Geophys. Fluid Dyn.* **3**, 211 (1972).
- [7] K. Amara and J. Hegseth, Convection in a spherical capacitor, *J. Fluid Mech.* **450**, 297 (2002).
- [8] P. H. Roberts, Electrohydrodynamic convection, *Q. J. Mech. Appl. Math.* **22**, 211 (1969).
- [9] F. Zaussinger, P. Haun, P. S. B. Szabo, V. Travnikov, M. Al Kawwas, and C. Egbers, Rotating spherical gap convection in the GeoFlow International Space Station (ISS) experiment, *Phys. Rev. Fluids* **5**, 063502 (2020).
- [10] J. E. Hart, G. A. Glatzmaier, and J. Toomre, Space-laboratory and numerical simulations of thermal convection in a rotating hemispherical shell with radial gravity, *J. Fluid Mech.* **173**, 519 (1986).
- [11] J. E. Hart, J. Toomre, A. E. Deane, N. E. Hurlburt, G. A. Glatzmaier, G. H. Fichtl, F. Leslie, W. W. Fowles, and P. A. Gilman, Laboratory experiments on planetary and stellar convection performed on Spacelab 3, *Science* **234**, 61 (1986).
- [12] P. Beltrame, V. Travnikov, M. Gellert, and C. Egbers, GEOFLOW: Simulation of convection in a spherical shell under central force field, *Nonlinear Processes Geophys.* **13**, 413 (2006).
- [13] M. Gellert, P. Beltrame, and C. Egbers, The GeoFlow experiment: Spherical Rayleigh-Bénard convection under the influence of an artificial central force field, *J. Phys.* **14**, 157 (2005).
- [14] J. T. Karlsen, P. Augustsson, and H. Bruus, Acoustic Force Density Acting on Inhomogeneous Fluids in Acoustic Fields, *Phys. Rev. Lett.* **117**, 114504 (2016).
- [15] J. P. Koulakis, S. Pree, A. Thornton, A. S. Nguyen, and S. Putterman, Pycnoclinic acoustic force, *Proc. Meetings Acoustics* **34**, 045005 (2018).
- [16] J. P. Koulakis and S. Putterman, Convective instability in a stratified ideal gas containing an acoustic field, *J. Fluid Mech.* **915**, A25 (2021).
- [17] G. Z. Gershuni and D. V. Lyubimov, *Thermal Vibrational Convection* (John Wiley & Sons Ltd., West Sussex, England, 1998), pp. 249–250.
- [18] See Supplemental Material at <http://link.aps.org/supplemental/10.1103/PhysRevLett.130.034002> for high speed video of the convection events analyzed herein.

- [19] J. P. Koulakis, S. Pree, A. L. F. Thornton, and S. Putterman, Trapping of plasma enabled by pycnoclinic acoustic force, *Phys. Rev. E* **98**, 043103 (2018).
- [20] J. P. Koulakis, S. Pree, and S. Putterman, Acoustic resonances in gas-filled spherical bulb with parabolic temperature profile, *J. Acoust. Soc. Am.* **144**, 2847 (2018).
- [21] S. Lepot, S. Aumaitre, and B. Gallet, Radiative heating achieves the ultimate regime of thermal convection, *Proc. Natl. Acad. Sci. U.S.A.* **115**, 8937 (2018).
- [22] D. Goluskin, *Internally Heated Convection and Rayleigh-Bénard Convection* (Springer International Publishing, Switzerland, 2016).
- [23] S. Pree, J. Koulakis, A. Thornton, and S. Putterman, Acousto-convective relaxation oscillation in plasma lamp, *Proc. Meetings Acoustics* **34**, 045015 (2018).
- [24] J. P. Koulakis, S. Pree, and S. Putterman, Generation and characterization of chaotic convection in collisional plasma, *IEEE Trans. Plasma Sci.* **48**, 3840 (2020).
- [25] J. P. Koulakis, A. L. F. Thornton, and S. Putterman, Magnetron coupling to sulfur plasma bulb, *IEEE Trans. Plasma Sci.* **45** (2017).
- [26] G. Courret, P. Nikkola, S. Wasterlain, O. Gudozhnik, M. Girardin, J. Braun, S. Gavin, M. Croci, and P. W. Egolf, On the plasma confinement by acoustic resonance—an innovation for electrodeless high-pressure discharge lamps, *Eur. Phys. J. D* **71**, 214 (2017).
- [27] C. W. Johnston, H. W. P. van der Heijden, G. M. Janssen, J. van Dijk, and J. J. A. M. van der Mullen, A self-consistent LTE model of a microwave-driven, high pressure sulfur lamp, *J. Phys. D* **35**, 342 (2002).
- [28] C. W. Johnston, H. W. P. van der Heijden, A. Hartgers, K. Garloff, J. van Dijk, and J. J. A. M. van der Mullen, An improved LTE model of a high pressure sulfur lamp, *J. Phys. D* **37**, 211 (2004).
- [29] B. P. Turner, M. G. Ury, Y. Leng, and W. G. Love, Sulfur lamps—progress in their development, *J. Illum. Eng. Soc.* **26**, 10 (1997).
- [30] A. Zebib, G. Schubert, J. L. Dein, and R. C. Paliwal, Character and stability of axisymmetric thermal convection in spheres and spherical shells, *Geophys. Astrophys. Fluid Dyn.* **23**, 1 (1983).
- [31] B. Futterer, C. Egbers, N. Dahley, S. Koch, and L. Jehring, First identification of sub- and supercritical convection patterns from ‘GeoFlow’, the geophysical flow simulation experiment integrated in Fluid Science Laboratory, *Acta Astronaut.* **66**, 193 (2010).
- [32] T. Gastine, J. Wicht, and J. M. Aurnou, Turbulent Rayleigh-Bénard convection in spherical shells, *J. Fluid Mech.* **778**, 721 (2015).
- [33] S. Pree, S. Putterman, and J. P. Koulakis, Acoustic self-oscillation in a spherical microwave plasma, *Phys. Rev. E* **100**, 033204 (2019).
- [34] R. Menaut, Y. Corre, L. Hugué, T. Le Reun, T. Alboussiére, M. Bergman, R. Deguen, S. Labrosse, and M. Moulin, Experimental study of convection in the compressible regime, *Phys. Rev. Fluids* **4**, 033502 (2019).